

Unconventional parametric spin-wave pumping in single-crystal iron filmsShoki Nezu ¹, Thomas Scheike ², Hiroaki Sukegawa ², and Koji Sekiguchi ^{3,4,*}¹*Graduate School of Engineering Science, Yokohama National University, Tokiwadai 79-5, Yokohama 240-8501, Japan*²*National Institute for Materials Science, Sengen 1-2-1, Tsukuba, Ibaraki 305-0047, Japan*³*Institute of Advanced Science, Yokohama National University, Tokiwadai 79-5, Yokohama 240-8501, Japan*⁴*Faculty of Engineering, Yokohama National University, Tokiwadai 79-5, Yokohama 240-8501, Japan*

(Received 28 December 2023; revised 7 March 2024; accepted 3 April 2024; published 2 May 2024)

Spin waves hold promise for expanding the magnonics research field to include quantum information processing and classical information devices. Parametric pumping is considered a key technique to achieve this important advancement. Recently, a single-crystal iron has shown potential as a spin-wave excitation medium; however, parametric pumping in single-crystal iron films has not been investigated. In this study, we explored computationally and experimentally the characteristics of parametrically pumped spin waves in single-crystal iron thin films by respectively using large-scale micromagnetic simulations and a high-precision spectrum analyzer. The results demonstrate unconventional parametric pumping attributed to the competition between the anisotropic and excitation fields, emerging at external magnetic field and low power levels that would be insufficient to induce parametric pumping in isotropic materials. Systematic research on parametric pumping in iron could pave the way for low-energy spin-wave devices, enhancing quantum information device technology.

DOI: [10.1103/PhysRevB.109.184402](https://doi.org/10.1103/PhysRevB.109.184402)**I. INTRODUCTION**

Intensive research on spintronics revealed the profound importance of spin waves in the development of next-generation information processing. Spin waves can serve as noncharged information carriers and building blocks of broadband (gigahertz-terahertz) nanoscale processors [1–3]. As building blocks of broadband processors, propagating spin waves have been used to successfully implement various rf functionalities, such as transistors [4], logic circuits [5–8], multiplexers [9], directional couplers [10], and switches [11,12]. In addition to these classical rf functionalities, spin waves can be applied to quantum information processing [13,14] as magnons, the quanta of spin waves, exhibit Bose-Einstein condensation (BEC) [15,16], and magnon quantum condensates can provide some functionality of quantum bits (qubits) [17] even at room temperature. The field of quantum magnonics has received considerable attention recently, prompting vigorous research efforts. These endeavors, including low-temperature quantum [18,19] and hybrid magnonics [20–22], have paved the way for the exploration of magnons and yttrium iron garnet (YIG) films composed of a well-understood material with small magnetic damping (equally long magnon lifetime) [23–25]. However, the research findings on magnonic qubits have not yet been firmly established. The challenges associated with magnonic qubit research arise from the competition between the efficiency of the magnon generation method and the thermal agitation of the environment. To generate a magnon quantum condensate, a nonlinear, high-power rf excitation of spin waves, known

as parametric pumping, is essential [26]. However, parametric pumping unavoidably induces a thermal energy flow in the BEC medium, thus leading to thermal agitation enhancements. It is noteworthy that YIG has a modest saturation magnetization ($M_s = 140$ kA/m [27–29]), and the thermal effects on M_s become significant. The spin-wave resonance (the condition for magnon generation) in YIG is particularly susceptible to thermal agitations [30–32].

Recently, an alternative approach to the magnonic qubit has been suggested that utilizes single-crystal iron (Fe) thin films prepared by epitaxial growth on single-crystal substrates as a BEC medium [33,34]. The typical saturation magnetization of a single-crystal Fe(001) thin film is $M_s = 1.6$ MA/m, approximately 11 times larger than that of YIG [35,36]. While the magnon lifetime in single-crystal Fe is shorter compared with that in YIG, the in-plane magnetic anisotropy due to its cubic magnetocrystalline anisotropy of Fe compensates for the group velocity, decay length, and spin-wave amplitude [36,37]. The possibility of magnon condensation in single-crystal Fe has been reported under specific conditions; however, the relationship between the efficiency of parametric pumping and the cubic anisotropy axis, and the detailed dynamics of parametrically excited spin waves in single-crystal Fe thin films, remain to be elucidated. An investigation into magnon generation through parametric pumping is crucial for the development of magnonic qubits using single-crystal Fe thin films.

In this study, the parametric pumping process of spin waves in single-crystal Fe thin films was investigated in detail using a spectrum analyzer. All-electric detection using a spectrum analyzer is more sensitive and provides better frequency-domain resolution compared with the direct current (dc) spin-Hall effect [38–40], as there is no spin-current conversion. The

Corresponding author: sekiguchi-koji-gb@ynu.ac.jp

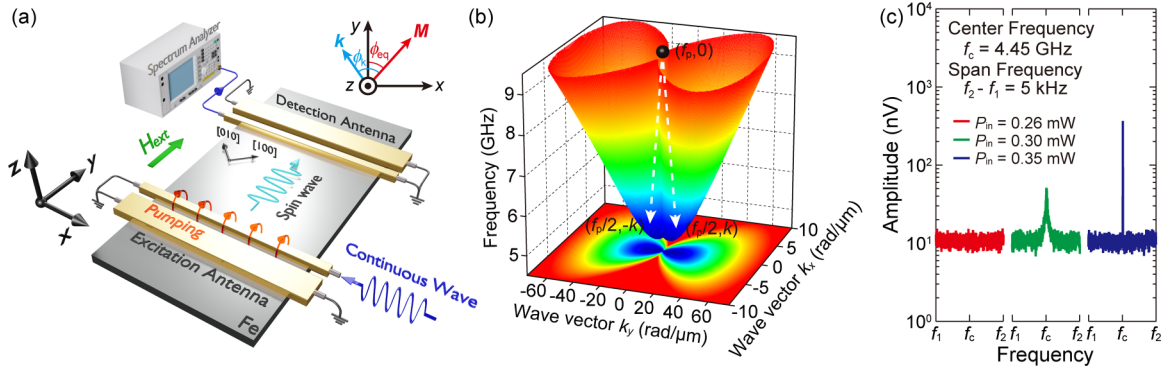


FIG. 1. Schematic of the experimental setup and the mechanism of the parametric pumping process. (a) Diagram depicting the parametric pumping measurements. A continuous wave was launched into the excitation antenna, and parametrically excited spin waves were observed by the detection antenna with the spectrum analyzer. The external magnetic fields were applied parallel to the hard axis direction of the Fe films (y direction). The inset within the top right depicts the utilized coordinate system. The angles ϕ_k and ϕ_{eq} represent the angle between the magnetization \mathbf{M} and the wave vector \mathbf{k} , and \mathbf{M} and the y axis, respectively. (b) Illustration of the dispersion relation of spin waves and the parametric pumping process. Spin waves with a frequency of $f_p/2$ and wave number of $\pm k$ are generated by a pumping field with a frequency of f_p . (c) The amplitudes of parametrically pumped spin waves at different excitation powers $P_{in} = 0.26, 0.30,$ and 0.35 mW. The pumping frequency and external field were set to $f_p = 8.90$ GHz and $\mu_0 H_{ext} = 80$ mT, respectively. The center and span frequencies were set to $f_c = f_p/2 = 4.45$ GHz and $f_2 - f_1 = 5$ kHz, respectively.

number of magnons generated by parametric pumping was directly evaluated based on the spectral peak of the spin-wave amplitude as a function of the bias magnetic field and pumping power. Systematic experiments revealed the existence of three different bias fields, i.e., triggering points, for a given pumping frequency. At these triggering points, a larger efficiency (ten times) of parametric pumping was achieved. In combination with micromagnetic simulations, the enhancement of pumping efficiency was found to originate from the cubic anisotropy of Fe. These results shed light on a promising path for additional magnonic qubit research.

II. RESULTS AND DISCUSSION

Figure 1(a) shows a schematic of the experimental setup. The spin-wave medium was deposited on a MgO(001) single-crystal substrate. A highly (001)-oriented single-crystal Fe film was deposited with a Cr(001) buffer and a MgAl₂O₄(001) cap. The whole stack structure is Cr (40)/Fe (25)/MgAl₂O₄ (~ 2 ; thickness in nanometers) [35]. The deposition was conducted at room temperature using a dc/rf ultrahigh-vacuum magnetron sputtering system with a base pressure of less than 7×10^{-7} Pa. The Cr buffer and Fe layer were *in situ* post-annealed at 700 °C and 300 °C, respectively, to ensure an atomically flat surface and a highly (001) orientation. The MgAl₂O₄ cap was prepared by natural oxidation of a Mg (0.45 nm)/Mg₁₉Al₈₁ (1.2 nm) bilayer. The magnetic properties of the single-crystal Fe(001) film were characterized using a vibrating sample magnetometer, revealing the saturation magnetization [$M_s = (1.6 \pm 0.1) \times 10^6$ A/m] and the in-plane magnetic anisotropy field $\mu_0 H_{ani} = (66 \pm 2)$ mT [36]. The Fe(001) film was patterned into a rectangle using an Ar ion milling technique. The dimensions of the rectangle were 180 μ m in length and 110 μ m in width. The longitudinal axis (y axis) of the sample was aligned parallel to the hard axis, i.e., Fe[110].

A pair of asymmetric coplanar transmission lines was created using a 5-nm Ti adhesive layer and a 200-nm Au layer using vacuum deposition and liftoff processes. The transmission lines were designed with a signal width of 1.0 μ m and a gap width of 0.9 μ m, resulting in a characteristic impedance of 50 Ω . The separation distance between the transmission lines was designed to be 5 μ m and corresponded to the propagation length of spin waves. Spin waves were parametrically excited by an excitation transmission line launching a microwave field h_p at frequency f_p using a signal generator (Agilent Technologies, 83732B). An external magnetic field H_{ext} was applied parallel to the hard axis, and a signal of pumped spin waves was detected by a detection transmission line connected to a precision spectrum analyzer (Agilent Technologies, E4440A). The opposite ends of both the excitation and the detection transmission lines were connected to a low-noise ground plane (GND). The measured signal $V(f)$ was composed of the pumped spin-wave amplitude V_{sw} and background noise V_n , and can be represented as $V(f) = V_{sw} + V_n$. The center and span frequencies of the spectrum analyzer were set at $f_p/2$ (half the pumped frequency) and 5 kHz, respectively. Note that the unfavorable electromagnetic interference induced voltage by the excitation antenna at f_p was eliminated with this condition as the parametrically excited spin-wave signals possess the frequency of $f_p/2$.

To understand the parametric pumping process in single-crystal Fe films, the dispersion of a single-crystal Fe film was calculated [Fig. 1(b)] using the parameters $M_s = 1.6$ MA/m, $\mu_0 H_{ani} = 66$ mT, thickness $d = 25$ nm, and $\mu_0 H_{ext} = 80$ mT. In this saturation condition ($H_{ext} > H_{ani}$), the magnetization \mathbf{M} aligns with the direction of the external magnetic field, and the dispersion simply represents the relationship of the spin-wave resonance frequency f versus the wave vectors k_y and k_x , which are y - and x -axis components of the wave vector \mathbf{k} , respectively. In linear spin-wave excitations, a microwave field h_p must be matched with the spin-wave resonance

frequency at a given external magnetic field. However, when the amplitude of the microwave field is large enough to overcome spin-wave relaxation, spin-wave excitation becomes possible at microwave fields at frequencies other than the resonant frequency. In this high-power (nonlinear) excitation of the spin waves, the magnetic system allows parametric pumping. There are two typical mechanisms for the parametric excitation of spin waves: parallel and perpendicular pumping [41,42]. In the case of parallel pumping ($\mathbf{M}||h_p$), spin waves at the frequency $f_p/2$ are directly excited by the parallel component of microwave fields at the frequency f_p . In the case of perpendicular pumping ($\mathbf{M}\perp h_p$), spin waves at the frequency $f_p/2$ are excited by the nonresonant magnetization precession, which is induced by the perpendicular component of the microwave field. In both cases, a pair of spin waves with opposite wave vectors (\mathbf{k} and $-\mathbf{k}$) were generated at the frequency $f_p/2$, obeying the momentum and energy conservation law. Figure 1(c) exemplifies the parametric pumping at $\mu_0 H_{\text{ext}} = 80$ mT. The excitation frequency and the center frequency of the spectrum analyzer were set to $f_p = 8.90$ GHz and $f_c = f_p/2 = 4.45$ GHz, respectively. The signals $V(f)$ represent the parametrically pumped spin-wave amplitudes and their dependence on pumping power. At a low input power ($P_{\text{in}} = 0.26$ mW), the signal only consists of a background noise $V_n \sim 10$ nV. As the input power increases to $P_{\text{in}} = 0.30$ mW, a distinct peak with a broad linewidth emerges at the center frequency $f_p/2$. At higher power levels ($P_{\text{in}} = 0.35$ mW), the peak becomes sharp, thus indicating the presence of parametric pumping.

In a generalized case at a specific H_{ext} , the spin-wave resonance frequency f for the cubic anisotropic Fe film is described by the following equation [36,37,43]:

$$f = \frac{\gamma_g \mu_0}{2\pi} \sqrt{H_1 H_2}, \quad (1)$$

where the gyromagnetic ratio is $[\gamma_g = 1.76 \times 10^6 \text{ T}^{-1} \text{ s}^{-1}]$. The in-plane effective magnetic field H_1 and normal effective magnetic field H_2 can be expressed as

$$H_1 = H_{\text{ext}} \cos \phi_{\text{eq}} - H_{\text{ani}} \cos(4\phi_{\text{eq}}) + \frac{2A_{\text{exch}}}{M_s} k^2 + M_s P_k \sin^2 \phi_k, \quad (2)$$

$$H_2 = H_{\text{ext}} \cos \phi_{\text{eq}} + H_{\text{ani}} + \frac{2A_{\text{exch}}}{M_s} k^2 + M_s (1 - P_k), \quad (3)$$

where the saturation magnetization $M_s = 1.6$ MA/m, the cubic anisotropy field $\mu_0 H_{\text{ani}} = 66$ mT, the exchange constant $A_{\text{exch}} = 13$ pJ/m, $P_k = 1 - (1 - e^{-|k|d})/|k|d$, ϕ_k represents the angle between the magnetization \mathbf{M} and the wave vector \mathbf{k} , and ϕ_{eq} denotes the angle between the magnetization \mathbf{M} and the y axis [inset in Fig. 1(a)]. The angle $\phi_{\text{eq}} = 0$ for $h \geq 1$, $h = H_{\text{ext}}/H_{\text{ani}}$, and

$$\phi_{\text{eq}} = \frac{\pi}{2} - \sin^{-1} \left(\frac{6^{1/3} + (9h + \sqrt{81h^2 - 6})^{2/3}}{6^{2/3}(9h + \sqrt{81h^2 - 6})^{1/3}} \right) \quad (4)$$

for $0 \leq h < 1$. In this experiment, an external magnetic field was applied parallel to the hard magnetization axis. Therefore, in Fe films with $H_{\text{ext}} < H_{\text{ani}}$, the parametric pumping becomes intermediate between parallel and perpendicular pumping and is known as oblique pumping. At $H_{\text{ext}} > H_{\text{ani}}$, the magnetization aligns parallel to the external field. However, since a

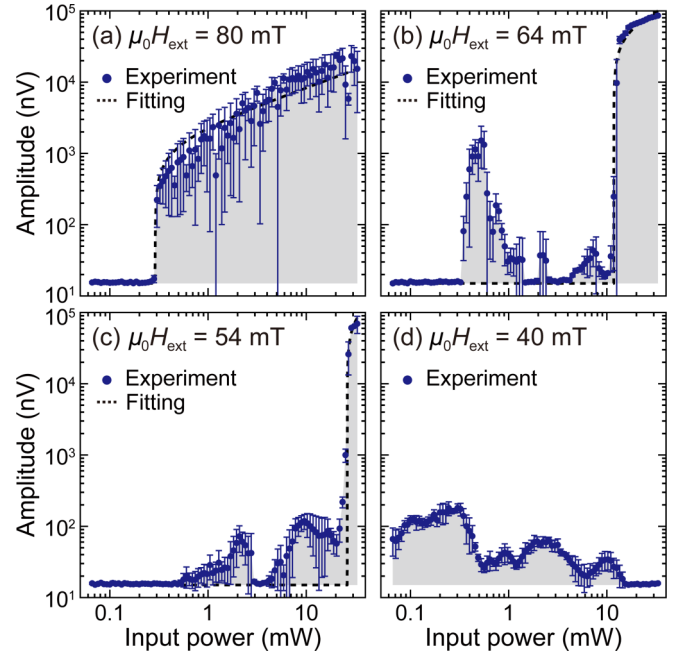


FIG. 2. Generation of parametrically excited spin waves measured at $f_p/2 = 4.45$ GHz. Excitation power dependencies of parametrically pumped spin-wave amplitudes at the pumping frequency $f_p = 8.90$ GHz and the various external magnetic fields: (a) 80 mT, (b) 64 mT, (c) 54 mT, and (d) 40 mT. The broken lines correspond to the theoretical fittings. At each excitation power measurement, five independent measurements were performed. The data points represent the mean values, and the error bars represent the standard deviations of the measurements.

coplanar transmission line is used for parametric pumping in this study, spin waves are not excited only by pure parallel pumping. Notably, an increase in the external magnetic field induces a transition from parallel to perpendicular pumping [44]. This phenomenon is attributed to the spatial localization of the pump field, specifically the microwave magnetic field components perpendicular to the film plane at the sides of the coplanar transmission line.

Figure 2 represents the excitation power dependence of the parametrically pumped spin-wave amplitude with a frequency of $f_p/2$ at various external magnetic fields. The excitation frequency was fixed to $f_p = 8.90$ GHz. As shown in Fig. 2(a), by increasing the excitation power from 66 μW to 32 mW at $\mu_0 H_{\text{ext}} = 80$ mT, the pumped spin-wave amplitude exhibits a threshold, and the spin-wave amplitude changes the order of magnitude. According to the theory of parametric excitation, the pumped spin-wave amplitude V_{sw} is proportional to the $\sqrt{P_{\text{in}} - P_{\text{th}}}$, where P_{in} and P_{th} are input and threshold powers, respectively [45,46]. The experimental result was analyzed using the following equation:

$$V = a\sqrt{P_{\text{in}} - P_{\text{th}}} + V_n, \quad (5)$$

where a is a fitting parameter. The fitting deduced the threshold power $P_{\text{th}} = 0.29$ mW and shows excellent agreement as indicated by the broken line. By reducing the external magnetic field to $\mu_0 H_{\text{ext}} = 64$ mT, we examined oblique

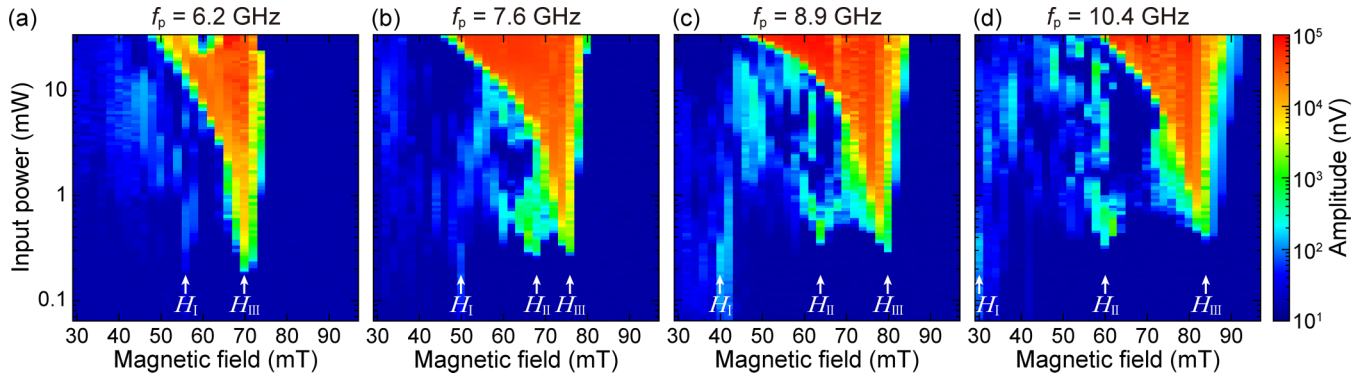


FIG. 3. Experimental threshold characteristics of parametric pumping. The amplitudes of parametrically excited spin waves with a frequency of $f_p/2$ were measured at three distinct pumping frequencies: (a) 6.2 GHz, (b) 7.6 GHz, (c) 8.9 GHz, and (d) 10.4 GHz. The external magnetic field and excitation power were changed in the range $30 \leq H_{\text{ext}} \leq 96$ mT and $66 \mu\text{W} \leq P_{\text{in}} \leq 32$ mW. H_I , H_{II} , and H_{III} represent the characteristic fields that exhibit parametric pumping at low input power levels.

pumping in the single-crystal Fe film. As shown in Fig. 2(b), we observed that the pumped signal exhibited an additional change at $P_{\text{in}} = 0.46$ mW and had an amplitude of 10^3 nV. The pumping at $P_{\text{th}} = 11.7$ mW increased the amplitude to 10^5 nV; the change can be explained by Eq. (5). In the case of $\mu_0 H_{\text{ext}} = 54$ mT, additional changes appear when $P_{\text{in}} = 0.56$ mW and $P_{\text{in}} = 4.2$ mW, and the pumping of 10^5 nV appears at the higher threshold $P_{\text{th}} = 26.1$ mW. Remarkably, in a weaker magnetic field $\mu_0 H_{\text{ext}} = 40$ mT, the spin-wave amplitude was enhanced considerably to 66.2 nV at a very low input power [$P_{\text{in}} = 66 \mu\text{W}$], even though the pumping observed at 10^5 nV was lost.

The parametric excitation of spin waves in the cubic anisotropic Fe films was systematically investigated by constructing and analyzing the color plot of spin-wave amplitudes as functions of input power P_{in} and external magnetic field H_{ext} . Figure 3 shows the color plot of spin-wave amplitudes with a frequency of $f_p/2$ at various pumping frequencies f_p . The striking characteristic of the V-shaped structure shown in each panel is known as an asymmetric butterfly curve. However, the butterfly curve is not the same as previously reported [47,48]. In the case of $f_p = 6.2$ GHz as shown in Fig. 3(a), the threshold power gradually decreased from 32 to 0.19 mW as the magnetic field increased along the

butterfly curve. Once the external magnetic field reached a characteristic field of 70 mT (labeled III, H_{III}), a minimal increase in H_{ext} of only 4 mT triggered a rapid rise in the threshold power back to 32 mW. This occurred because half the pumping frequency $f_p/2$ deviated from the spin-wave dispersion branch, disabling parametric pumping. Note that there is another remarkable field at $\mu_0 H_{\text{ext}} = 56$ mT (labeled I, H_I) where parametric pumping is achieved at a low input power ($P_{\text{in}} = 66 \mu\text{W}$), implying a slightly higher pumping efficiency. At other pumping frequencies $f_p = 7.6$ GHz [Fig. 3(b)], 8.9 GHz [Fig. 3(c)], and 10.2 GHz [Fig. 3(d)], the characteristic fields were also observed and labeled as H_I , H_{II} , and H_{III} in each panel. The detailed values of characteristic magnetic fields are summarized in Table I. These fields correspond to the field where additional changes are observed in Fig. 2.

The origin of characteristic fields could be explained by the parametric instability that was revealed by pioneering works [44,49,50]. The parametric instability indicates that the parametric pumping shows a maximum efficiency when half the pumping frequency $f_p/2$ becomes equivalent to the ferromagnetic resonance (FMR) frequency f_{FMR} . Using Eqs. (1)–(3) and setting $k = 0$, the FMR frequency of the cubic anisotropic Fe film can be expressed as

$$f_{\text{FMR}} = \frac{\gamma_g \mu_0}{2\pi} \sqrt{[H_{\text{ext}} \cos \phi_{\text{eq}} - H_{\text{ani}} \cos(4\phi_{\text{eq}})](H_{\text{ext}} \cos \phi_{\text{eq}} + H_{\text{ani}} + M_s)}. \quad (6)$$

Using Eq. (6), we calculated the characteristic fields for each pumping frequency; the values are summarized in Table I. Note that Eq. (6) has two independent solutions ($\mu_0 H_{c2}$, $\mu_0 H_{c3}$). Comparing the calculated characteristic fields with the experimentally observed field, it is obvious that $\mu_0 H_{c2}$ and $\mu_0 H_{c3}$ agree with H_{II} and H_{III} , respectively. The threshold power P_{th} at H_{II} and H_{III} increases as pumping frequency increases, exhibiting a parametric instability feature.

Furthermore, we focused on the magnetic field labeled H_I , where enhanced spin waves were observed at an extremely low input power. For instance, when $f_p = 8.90$ GHz, the spin-wave amplitude was enhanced at $P_{\text{in}} = 66 \mu\text{W}$. Note that the

characteristic field H_I decreases as the pumping frequency increases. As the characteristic field appeared at a lower magnetic field, the possibility of three-magnon scattering was investigated. Three-magnon scattering refers to a nonlinear process in which three magnons interact with each other, and involves two processes: splitting, where one magnon splits into two, and confluence, where two magnons merge into one. Using Eq. (6) and the condition $f_{\text{FMR}} = f_p$ and $k \sim 0$, the characteristic fields $\mu_0 H_{c1}$ were calculated for each excitation frequency. As shown in Table I, the magnitudes of the characteristic field H_I were in good agreement with the calculations, with the only exception being the case of $f_p = 10.4$ GHz.

TABLE I. Experimentally determined and calculated characteristic magnetic fields.

f_p (GHz)	Experiment			Calculation		
	$\mu_0 H_I$ (mT)	$\mu_0 H_{II}$ (mT)	$\mu_0 H_{III}$ (mT)	$\mu_0 H_{c1}$ (mT)	$\mu_0 H_{c2}$ (mT)	$\mu_0 H_{c3}$ (mT)
6.20	56		70	53.7	63.1	71.7
7.60	50	68	76	46.5	61.6	74.6
8.90	40	64	80	37.3	59.9	77.7
10.4	30	60	84	18.1	57.5	82.0

The reason for this mismatch could be that experimentally, the external magnetic field was limited in the range $30 \text{ mT} \leq \mu_0 H_{\text{ext}} \leq 96 \text{ mT}$. Our observations consequently reveal an unconventional parametric pumping, emerging at external magnetic field and power levels that would be insufficient to induce parametric pumping in isotropic materials.

To understand the dynamics of this unconventional efficient parametric pumping in the Fe films, we performed micromagnetic simulations by numerically solving the Landau-Lifshitz-Gilbert equation, $\partial \mathbf{m} / \partial t = -\gamma_{\text{g}} \mu_0 \mathbf{m} \times \mathbf{H}_{\text{eff}} + \alpha_{\text{G}} \mathbf{m} \times \partial \mathbf{m} / \partial t$, using MUMAX3 [51]. In this equation, \mathbf{m} represents the unit vector along the magnetization, \mathbf{H}_{eff} encompasses the effective magnetic field components, including exchange, magnetostatic, and external magnetic fields, and α_{G} denotes the Gilbert damping constant. The thin Fe film was simulated with a unit cell $10 \text{ nm} \times 10 \text{ nm} \times 25 \text{ nm}$. The grid size was specified as $(N_x, N_y, N_z) = (600, 600, 1)$ with periodic boundary conditions denoted as $(P_x, P_y, P_z) = (512, 256, 0)$. The material parameters for the single-crystal Fe film were cubic anisotropy $K_c = 54.8 \text{ kJ/m}^3$, saturation magnetization $M_s = 1.6 \text{ MA/m}$, Gilbert damping constant $\alpha_{\text{G}} = 0.002$, and exchange stiffness constant $A_{\text{exch}} = 13 \text{ pJ/m}$. Detailed descriptions are available in the Supplemental Material [52].

The color plots of the parametrically pumped spin-wave intensities with a frequency of $f_p/2$ were reproduced in simulations using the pumping frequencies $f_p = 6.2, 7.6, 8.9$, and 10.4 GHz , and the simulated results are shown in Fig. 4. As observed, the butterfly curves (shown in red and green) are not identical to the experimental results; the butterfly curve values did not decrease to $P_{\text{th}} = 0.19 \text{ mW}$ but to 2.3 mW .

Except for this point, the simulation results reproduced the experimentally obtained pumping characteristics. As shown in Figs. 4(a)–4(d), H_I , H_{II} , and H_{III} are characteristic fields, and the threshold power P_{th} was reduced. These simulation values of H_I , H_{II} , and H_{III} are in agreement with the experimental results and the calculated characteristic fields $\mu_0 H_{c1}$, $\mu_0 H_{c2}$, and $\mu_0 H_{c3}$. Similar to the experimental results, the unconventional characteristic field H_I decreases as the pumping frequency increases. Notably, in the cases of $f_p = 8.9 \text{ GHz}$ and $f_p = 10.4 \text{ GHz}$, the simulations predicted the existence of another characteristic field H_{IV} . As shown in Figs. 4(c) and 4(d), the values of H_{IV} were close to the magnetocrystalline anisotropy field H_{ani} . However, this field was not observed experimentally. This could be the reason that experimentally, in a backward volume configuration, spin waves cannot propagate for $5 \mu\text{m}$ in single-crystal Fe thin films at $H_{\text{ext}} = H_{\text{ani}}$, while the simulation focused the parametric excitation process underneath the excitation transmission line (within $2 \mu\text{m}$ length) [37].

Figure 5 exemplifies spin-wave generation under parametric pumping in simulations. Each panel is the frequency cross section of spin-wave dispersion, as shown in Fig. 1(b). The pumping frequency and power were fixed at $f_p = 8.9 \text{ GHz}$ and $P_{\text{in}} = 0.22 \text{ mW}$, respectively. Figures 5(a)–5(d) represent spin-wave intensities at the pumping frequency $f_p = 8.9 \text{ GHz}$, while Figs. 5(e)–5(h) represent intensities at the pumped frequency $f_p/2 = 4.45 \text{ GHz}$. The pink lines show the theoretical dispersion relations. At the weak field $\mu_0 H_{\text{ext}} = 36 \text{ mT}$ (H_I), spin-wave generation was dominated by the red region on the dispersion branch at $f_p = 8.9 \text{ GHz}$ and $k \sim 0$ [Fig. 5(a)]. Although no dispersion branch exists at $f_p/2 =$

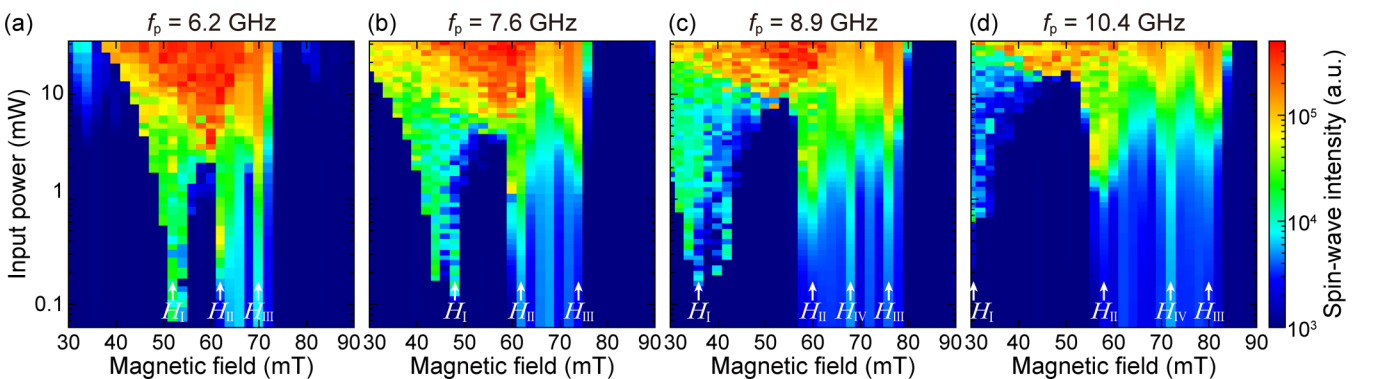


FIG. 4. Simulated threshold characteristics of parametric pumping. The intensities of parametrically excited spin waves with a frequency of $f_p/2$ were simulated at four distinct pumping frequencies: (a) 6.2 GHz, (b) 7.6 GHz, (c) 8.9 GHz, and (d) 10.4 GHz. The external magnetic field and excitation power were changed in the range $30 \leq H_{\text{ext}} \leq 90 \text{ mT}$ and $66 \mu\text{W} \leq P_{\text{in}} \leq 32 \text{ mW}$. H_I , H_{II} , H_{III} , and H_{IV} represent the characteristic fields that exhibit parametric pumping at low input power levels.

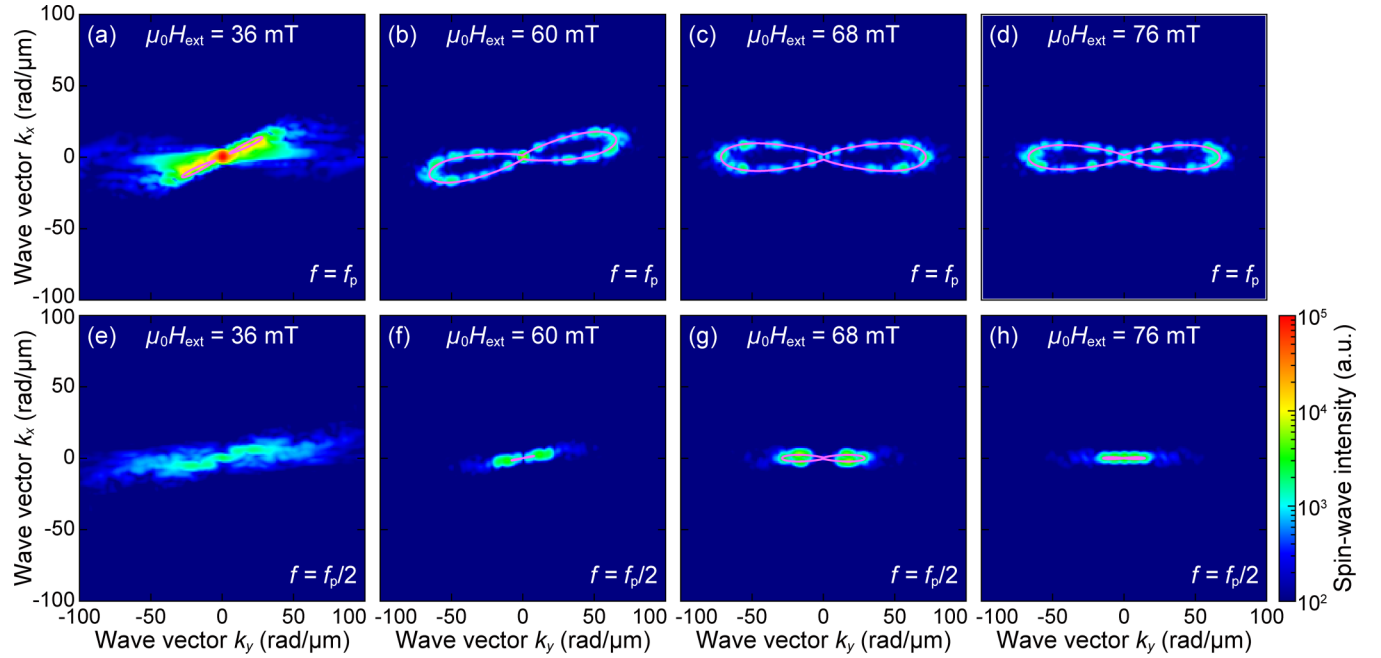


FIG. 5. Spin-wave generation under parametric pumping conditions. Spin-wave intensities at the pumping frequency $f_p = 8.90$ GHz (a)–(d) and the pumped frequency $f_p/2 = 4.45$ GHz (e)–(h) in simulations. Each panel represents the frequency cross section of spin-wave dispersion. The input power was $P_{in} = 0.22$ mW. The external magnetic fields were, (a),(e) 36 mT, (b),(f) 60 mT, (c),(g) 68 mT, and (d), (h) 76 mT. The pink lines show the theoretical dispersion relations.

4.45 GHz [Fig. 5(e)], the presence of scattered spin waves is undeniably evident, as manifested by the diffuse green stripe region extending along k_y . These scattered spin waves likely originate from the pump source, which consists of spin waves with a frequency of $f_p = 8.9$ GHz. As the external magnetic

field is increased, a theoretical dispersion emerges at $f_p/2 = 4.45$ GHz and $\mu_0 H_{ext} = 60$ mT (H_{II}) [Fig. 5(f)]. This signifies the initiation of parametric spin-wave generation. Additionally, weak spin waves with finite wave vectors ($k \neq 0$) are generated on the branch [Fig. 5(b)] of the ∞ -shaped structure

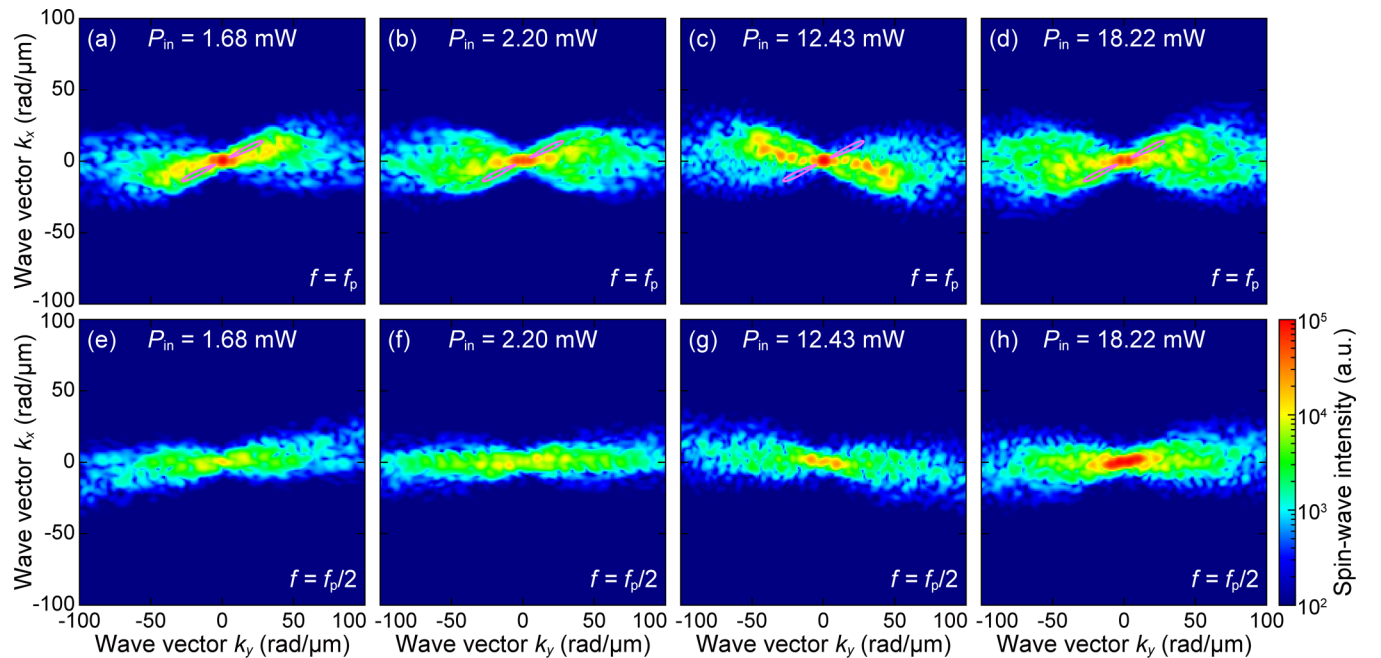


FIG. 6. Spin-wave generation under unconventional pumping conditions. Spin-wave intensities at the pumping frequency $f_p = 8.90$ GHz (a)–(d) and the pumped frequency $f_p/2 = 4.45$ GHz (e)–(h) in simulations. Each panel represents the frequency cross section of spin-wave dispersion. The external magnetic field was $\mu_0 H_{ext} = 36$ mT. The excitation powers were, (a),(e) 1.68 mW, (b),(f) 2.20 mW, (c),(g) 12.43 mW, and (d),(h) 18.22 mW. The pink lines delineate the theoretical dispersion relations at $\mu_0 H_{ext} = 36$ mT.

at $f_p = 8.9$ GHz through a second-order parametric process. When the external magnetic field exceeds the crystalline magnetic anisotropy field $\mu_0 H_{\text{ext}} > \mu_0 H_{\text{ani}} = 66$ mT, spin-wave generation is dominated at $f_p/2 = 4.45$ GHz [Figs. 5(g) and 5(h)] with 2.63- and 2.34-times stronger intensity than at $f_p = 8.9$ GHz [Figs. 5(c) and 5(d)].

The unconventional, efficient spin-wave generation at H_1 was caused by the competition between the anisotropic and excitation rf fields. The external magnetic field H_1 ($H_1 < H_{\text{ani}}$) was not strong enough to pin the direction of magnetization, and the magnetization was tilted by the rf field. The dispersion changed as a function of the excitation field. Figure 6 shows the transition of the dispersion relation as a function of the input rf power P_{in} . The pumping frequency and external magnetic field were fixed at $f_p = 8.9$ GHz and $\mu_0 H_{\text{ext}} = 36$ mT (H_1), respectively. As shown by Figs. 6(a) and 6(e), at the low input power of $P_{\text{in}} = 1.68$ mW, the spin waves were generated at $f_p = 8.9$ GHz along the theoretical ∞ -shaped dispersion indicated by pink lines, i.e., fixed magnetization angle ϕ_{eq} calculation. However, as the input power increases from 2.20 mW [Figs. 6(b) and 6(f)], 12.43 mW [Figs. 6(c) and 6(g)], and 18.22 mW [Figs. 6(d) and 6(h)], the strong generation points shown in red and yellow deviate from the ∞ -shaped dispersion. Additionally, as input power increases, the pumped spin waves at $f_p/2 = 4.45$ GHz become dominant even when $\mu_0 H_{\text{ext}} = 36$ mT (H_1). These simulation results demonstrate that the efficient spin-wave generation at H_1 is caused by the modulation of the magnetization angle due to the rf field.

Finally, we analyzed the modulation of the magnetization angle in the Fe thin film beneath the excitation transmission line in simulations. Figure 7(a) represents a snapshot of the magnetization directions in the $3 \mu\text{m} \times 3 \mu\text{m}$ region, 2.5 ns after the rf excitation. The external magnetic field and input power were $\mu_0 H_{\text{ext}} = 36$ mT (H_1) and $P_{\text{in}} = 18.2$ mW, respectively. As observed, the static component of magnetization at 2.5 ns varies across different locations in the Fe thin film, thus forming a multidomainlike structure. By deducing the magnetization angle $|\phi|$ between the magnetization \mathbf{m} and the y axis of each cell and averaging over the $3 \mu\text{m} \times 3 \mu\text{m}$ region, the ϕ_{avg} of magnetization was derived using the equation $\phi_{\text{avg}} = \sum |\phi| / (N_x N_y)$. As shown in Fig. 7(b), the ϕ_{avg} becomes smaller than the theoretical magnetization angle $\phi_{\text{eq}} = 26.3^\circ$, and the ϕ_{avg} changes from 25.8° to 15.1° as the input power increases from 0.32 to 31 mW. Note that each ϕ_{avg} represents an averaged value of the inhomogeneous distribution of magnetization angle, while the theoretical analysis yields a uniform magnetization angle ϕ_{eq} over the region of interest. Considering this rf modulation of ϕ_{avg} , the dispersion transition was revisited in Figs. 7(c)–7(e). When the input power was $P_{\text{in}} = 0.22$ mW [Fig. 7(c)], spin waves were generated at the pumping frequency $f_p = 8.9$ GHz. According to the evaluation listed above, the angle was $\phi_{\text{avg}} = 25.1^\circ$, and the theoretical dispersion branch, shown by the white broken line, was located at 8.20 GHz and did not reach the parametric pumped frequency $f_p/2 = 4.45$ GHz. When the power increased to $P_{\text{in}} = 2.20$ mW [Fig. 7(d)], the angle was modulated to the value of $\phi_{\text{avg}} = 21.4^\circ$, and the theoretical dispersion branch was reduced to 6.66 GHz. When the power was $P_{\text{in}} = 18.2$ mW [Fig. 7(e)], the angle decreased

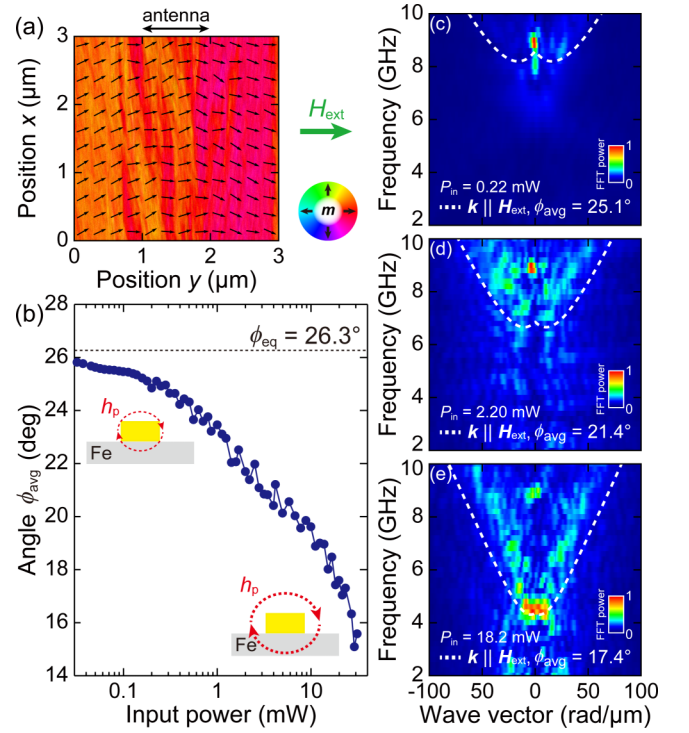


FIG. 7. Modulation of magnetization angle under unconventional pumping conditions. (a) Simulated snapshot of magnetization directions in the $3 \mu\text{m} \times 3 \mu\text{m}$ region underneath the excitation antenna at 2.5 ns after the rf excitation with $f_p = 8.9$ GHz, $P_{\text{in}} = 18.2$ mW, and $\mu_0 H_{\text{ext}} = 36$ mT. (b) Averaged magnetization angle ϕ_{avg} computed by varying the input power from 32 μW to 31 mW. The black dotted line is the theoretically obtained uniform magnetization angle $\phi_{\text{eq}} = 26.3^\circ$. (c)–(e) Transition of spin-wave dispersions by rf excitation at $P_{\text{in}} = 0.22$, 2.20, and 18.2 mW. The white broken lines show the dispersion relations calculated with the averaged magnetization angle ϕ_{avg} .

further to $\phi_{\text{avg}} = 17.4^\circ$, and the branch frequency became $f_p/2 = 4.45$ GHz. As shown in Fig. 7(e), the strong generation points (shown in red) are switched to approximately $f_p/2 = 4.45$ GHz, thus demonstrating parametric pumping. The inhomogeneous distribution of magnetization under the radiation of the rf field induced the unconventional parametric pumping process. Under the condition that the propagating direction of the spin waves aligns with the easy axis, we will lose the competition between the anisotropic and excitation radio-frequency fields, disabling the observation of unconventional parametric pumping. The anisotropic field, aligned in the same direction as the external magnetic field, simply strengthens the effective field, resulting in conventional parametric pumping observed in isotropic materials.

III. CONCLUSION

The parametric pumping process in cubic magnetic anisotropic Fe films was experimentally investigated using a high-precision spectrum analyzer. By detecting spin-wave intensities as a function of both the external magnetic field and the excitation power, three distinct characteristic fields (H_1 , H_{II} , and H_{III}) were identified at which parametric

pumping occurred at low power levels. The characteristic field H_I induces unconventional pumping at $f_{\text{FMR}} = f_p$ using the remarkably low input power of 66 μW . The characteristic fields H_{II} and H_{III} originated from the conventional parametric pumping at $f_{\text{FMR}} = f_p/2$. Large-scale micromagnetic simulations reproduced the experimental results and revealed that the competition between the anisotropic and excitation fields modulated the magnetization angle. The efficient unconventional pumping originated from the modulation of the magnetization angle. The advantage of single-crystal iron films lies in their noteworthy saturation magnetization, which is one order of magnitude higher than that of YIG films. This substantial saturation magnetization enables gigahertz/terahertz operation and enhances the temperature stability of magnonic devices. As demonstrated in this study, the in-plane magnetic anisotropy of single-crystal iron films facilitates unconventional parametric pumping at remarkably low power levels, unlocking the potential of these films as spin-wave media and transforming the landscape of magnonics. The details of parametric pumping characteristics

presented herein will contribute to future research efforts on magnonic qubits.

The data supporting the findings of this study are available from the corresponding author upon reasonable request.

ACKNOWLEDGMENTS

This work was supported by Grants-in-Aid for Scientific Research (Grants No. 19H00861, No. 18H05346, and No. 22K18321) from the Japanese Society for the Promotion of Science (JSPS). S.N. acknowledges the support of a Grant-in-Aid for JSPS Fellows (Grant No. 23KJ0989). K.S. acknowledges the support of Grants-in-Aid for Scientific Research (Grant No. 20H05652).

S.N. and K.S. planned the experiments. S.N., T.S., H.S., and K.S. designed and prepared the samples. S.N. performed parametrically excited spin-wave measurements and the micromagnetic simulations. S.N. and K.S. wrote the manuscript. All authors discussed the results.

The authors declare no competing financial interests.

-
- [1] K. Yamada, A. Hirohata, Y. Nakatani, I. L. Prejbeanu, B. Diény, P. Pirro, and B. Hillebrands, Review on spintronics: Principles and device applications, *J. Magn. Magn. Mater.* **509**, 166711 (2020).
- [2] S. A. Wolf, D. D. Awschalom, R. A. Buhrman, J. M. Daughton, S. Molnar, M. L. Roukes, A. Y. Chtchelkanova, and D. M. Treger, Spintronics: A spin-based electronics vision for the future, *Science* **294**, 1488 (2001).
- [3] K. Sekiguchi, The basis of magnon transistors, *AAPPS Bull.* **28**, 2 (2018).
- [4] A. V. Chumak, A. A. Serga, and B. Hillebrands, Magnon transistor for all-magnon data processing, *Nat. Commun.* **5**, 4700 (2014).
- [5] T. Goto, T. Yoshimoto, B. Iwamoto, K. Shimada, C. A. Ross, K. Sekiguchi, A. B. Granovsky, Y. Nakamura, H. Uchida, and M. Inoue, Three port logic gate using forward volume spin wave interference in a thin yttrium iron garnet film, *Sci. Rep.* **9**, 16472 (2019).
- [6] N. Kanazawa, T. Goto, K. Sekiguchi, A. B. Granovsky, C. A. Ross, H. Takagi, Y. Nakamura, H. Uchida, and M. Inoue, The role of Snell's law for a magnonic majority gate, *Sci. Rep.* **7**, 7898 (2017).
- [7] N. Sato, K. Sekiguchi, and Y. Nozaki, Electrical demonstration of spin-wave logic operation, *Appl. Phys. Express* **6**, 063001 (2013).
- [8] A. G. Khitun, M. Bao, and K. L. Wang, Magnonic logic circuits, *J. Phys. D: Appl. Phys.* **43**, 264005 (2010).
- [9] K. Vogt, F. Y. Fradin, J. E. Pearson, T. Sebastian, S. D. Bader, B. Hillebrands, A. Hoffmann, and H. Schultheiss, Realization of a spin-wave multiplexer, *Nat. Commun.* **5**, 3727 (2014).
- [10] Q. Wang, P. Pirro, R. Verba, A. Slavin, B. Hillebrands, and A. V. Chumak, Reconfigurable nanoscale spin-wave directional coupler, *Sci. Adv.* **4**, e1701517 (2018).
- [11] T. Meyer, T. Brächer, F. Heussner, A. A. Serga, H. Naganuma, K. Mukaiyama, M. Oogane, Y. Ando, B. Hillebrands, and P. Pirro, Realization of a spin-wave switch based on the spin-transfer-torque effect, *IEEE Magn. Lett.* **9**, 1 (2018).
- [12] M. Iwaba and K. Sekiguchi, Spin-wave switching using dynamic magnonic crystal, *Appl. Phys. Express* **14**, 073002 (2021).
- [13] T. Byrnes, K. Wen, and Y. Yamamoto, Macroscopic quantum computation using Bose-Einstein condensates, *Phys. Rev. A* **85**, 040306(R) (2012).
- [14] S. N. Andrianov and S. A. Moiseev, Magnon qubit and quantum computing on magnon Bose-Einstein condensates, *Phys. Rev. A* **90**, 042303 (2014).
- [15] S. O. Demokritov, V. Demidov, O. Dzyapko, G. A. Melkov, A. A. Serga, and B. Hillebrands, and A. N. Slavin, Bose-Einstein condensation of quasi-equilibrium magnons at room temperature under pumping, *Nature (London)* **443**, 430 (2006).
- [16] T. Giamarchi, C. Rüegg, and O. Tchernyshyov, Bose-Einstein condensation in magnetic insulators, *Nat. Phys.* **4**, 198 (2008).
- [17] M. Mohseni, V. I. Vasyuchka, V. S. L'vov, A. A. Serga, and B. Hillebrands, Classical analog of qubit logic based on a magnon Bose-Einstein condensate, *Commun. Phys.* **5**, 196 (2022).
- [18] S. Kosen, A. F. van Loo, D. A. Bozhko, L. Mihalceanu, and A. D. Karenowska, Microwave magnon damping in YIG films at millikelvin temperatures, *APL Mater.* **7**, 101120 (2019).
- [19] S. Knauer, K. Davidková, D. Schmoll, R. O. Serha, A. Voronov, Q. Wang, R. Verba, O. V. Dobrovolskiy, M. Lindner, T. Reimann *et al.*, Propagating spin-wave spectroscopy in a liquid-phase epitaxial nanometer-thick YIG film at millikelvin temperatures, *J. Appl. Phys.* **133**, 143905 (2023).
- [20] W. Han, S. Maekawa, and X.-C. Xie, Spin current as a probe of quantum materials, *Nat. Mater.* **19**, 139 (2020).
- [21] Y. Li, W. Zhang, V. Tyberkevych, W.-K. Kwok, A. Hoffmann, and V. Novosad, Hybrid magnonics: Physics, circuits, and applications for coherent information processing, *J. Appl. Phys.* **128**, 130902 (2020).

- [22] D. Lachance-Quirion, Y. Tabuchi, A. Gloppe, K. Usami, and Y. Nakamura, Hybrid quantum systems based on magnonics, *Appl. Phys. Express* **12**, 70101 (2019).
- [23] O. Dzyapko, V. E. Demidov, G. A. Melkov, and S. O. Demokritov, Bose–Einstein condensation of spin wave quanta at room temperature, *Philos. Trans. R. Soc., A* **369**, 3575 (2011).
- [24] A. A. Serga, V. S. Tiberkevich, C. W. Sandweg, V. I. Vasyuchka, D. A. Bozhko, A. V. Chumak, T. Neumann, B. Obry, G. A. Melkov, A. N. Slavin, and B. Hillebrands, Bose–Einstein condensation in an ultra-hot gas of pumped magnons, *Nat. Commun.* **5**, 3452 (2014).
- [25] M. Mohseni, A. Qaiumzadeh, A. A. Serga, A. Brataas, B. Hillebrands, and P. Pirro, Bose–Einstein condensation of nonequilibrium magnons in confined systems, *New J. Phys.* **22**, 083080 (2020).
- [26] V. S. L'vov, A. Pomyalov, D. A. Bozhko, B. Hillebrands, and A. A. Serga, Correlation-enhanced interaction of a Bose-Einstein condensate with parametric magnon pairs and virtual magnons, *Phys. Rev. Lett.* **131**, 156705 (2023).
- [27] M. C. Onbasli, A. Kehlberger, D. H. Kim, G. Jakob, M. Kläui, A. V. Chumak, B. Hillebrands, and C. A. Ross, Pulsed laser deposition of epitaxial yttrium iron garnet films with low Gilbert damping and bulk-like magnetization, *APL Mater.* **2**, 106102 (2014).
- [28] T. Liu, H. Chang, V. Vlaminck, Y. Sun, M. Kabatek, A. Hoffmann, L. Deng, and M. Wu, Ferromagnetic resonance of sputtered yttrium iron garnet nanometer films, *J. Appl. Phys.* **115**, 17A501 (2014).
- [29] S. F. Wang, K. Chorazewicz, S. Lamichhane, R. A. Parrott, S. Cabrini, P. Fischer, N. Kent, J. H. Turner, T. Ishibashi, Z. P. Frohock *et al.*, Ferromagnetic resonances in single-crystal yttrium iron garnet nanofilms fabricated by metal-organic decomposition, *Appl. Phys. Lett.* **119**, 172405 (2021).
- [30] B. Obry, V. I. Vasyuchka, A. V. Chumak, A. A. Serga, and B. Hillebrands, Spin-wave propagation and transformation in a thermal gradient, *Appl. Phys. Lett.* **101**, 192406 (2012).
- [31] J. Barker and G. E. W. Bauer, Thermal spin dynamics of yttrium iron garnet, *Phys. Rev. Lett.* **117**, 217201 (2016).
- [32] T. Eguchi, S. Nezu, Y. Naemura, and K. Sekiguchi, Spin-wave interconversion via thermoelectric point-contact control, *Phys. Rev. Res.* **4**, 033135 (2022).
- [33] K. Oda, M. Iwaba, and K. Sekiguchi, Time-resolved Brillouin light scattering study of magnon condensation, *Nippon Jiki Gakkai Kenkyukai Shiryo*, **235**, 13 (2022).
- [34] K. Oda, T. Scheike, H. Sukegawa, and K. Sekiguchi, Generating process of magnon Bose-Einstein condensation in cubic anisotropic materials, in The 83rd JSPS Autumn Meeting, Sendai, Japan (2022).
- [35] H. Sukegawa, Y. Miura, S. Muramoto, S. Mitani, T. Niizeki, T. Ohkubo, K. Abe, M. Shirai, K. Inomata, and K. Hono, Enhanced tunnel magnetoresistance in a spinel oxide barrier with cation-site disorder, *Phys. Rev. B* **86**, 184401 (2012).
- [36] K. Sekiguchi, S. W. Lee, H. Sukegawa, N. Sato, S. H. Oh, and R. D. McMichael, Spin-wave propagation in cubic anisotropic materials, *NPG Asia Mater.* **9**, e392 (2017).
- [37] S. Nezu, T. Scheike, H. Sukegawa, and K. Sekiguchi, Propagating backward-volume spin waves in epitaxial Fe films, *AIP Adv.* **12**, 035320 (2022).
- [38] H. Kurebayashi, O. Dzyapko, V. E. Demidov, D. Fang, A. J. Ferguson, and S. O. Demokritov, Spin pumping by parametrically excited short-wavelength spin waves, *Appl. Phys. Lett.* **99**, 162502 (2011).
- [39] A. V. Chumak, A. A. Serga, M. B. Jungfleisch, R. Neb, D. A. Bozhko, V. S. Tiberkevich, and B. Hillebrands, Direct detection of magnon spin transport by the inverse spin Hall effect, *Appl. Phys. Lett.* **100**, 082405 (2012).
- [40] T. B. Noack, V. I. Vasyuchka, D. A. Bozhko, B. Heinz, P. Frey, D. V. Slobodianiuk, O. V. Prokopenko, G. A. Melkov, P. Kopietz, B. Hillebrands, and A. A. Serga, Enhancement of the spin pumping effect by magnon confluence process in YIG/Pt bilayers, *Phys. Status Solidi B* **256**, 1900121 (2019).
- [41] H. J. Suhl, The theory of ferromagnetic resonance at high signal powers, *Phys. Chem. Solid* **1**, 209 (1957).
- [42] E. Schlömann, J. J. Green, and U. Milano, Recent developments in ferromagnetic resonance at high power levels, *J. Appl. Phys.* **31**, S386 (1960).
- [43] D. D. Stancil and A. Prabhakar, *Spin Waves: Theory and Applications* (Springer, New York, 2009).
- [44] T. Neumann, A. A. Serga, V. I. Vasyuchka, and B. Hillebrands, Field-induced transition from parallel to perpendicular parametric pumping for a microstrip transducer, *Appl. Phys. Lett.* **94**, 192502 (2009).
- [45] V. S. L'vov, *Wave Turbulence Under Parametric Excitation* (Springer, Berlin, Heidelberg, 1994).
- [46] C. W. Sandweg, Y. Kajiwara, A. V. Chumak, A. A. Serga, V. I. Vasyuchka, M. B. Jungfleisch, E. Saitoh, and B. Hillebrands, Spin pumping by parametrically excited exchange magnons, *Phys. Rev. Lett.* **106**, 216601 (2011).
- [47] T. Brächer, P. Pirro, B. Obry, B. Leven, A. A. Serga, and B. Hillebrands, Mode selective parametric excitation of spin waves in a Ni₈₁Fe₁₉ microstripe, *Appl. Phys. Lett.* **99**, 162501 (2011).
- [48] S. Hwang, S. Yoon, D. Seo, S. H. Han, and B. K. Cho, Parametric excitation and mode control using an Oersted field in a NiFe nanowire, *Sci. Rep.* **11**, 14207 (2021).
- [49] P. Kabos, M. Mendik, G. Wiese, and C. E. Patton, Spin-wave instability magnon distribution for parallel pumping in yttrium iron garnet films at 9.5 GHz, *Phys. Rev. B* **55**, 11457 (1997).
- [50] Y. H. Liu and C. E. J. Patton, Spin-wave instability threshold in single-crystal yttrium iron garnet for oblique pumping, *Appl. Phys.* **53**, 5116 (1982).
- [51] A. Vansteenkiste, J. Leliaert, M. Dvornik, M. Helsen, F. Garcia-Sanchez, and B. V. Waeyenberge, The design and verification of MuMax3, *AIP Adv.* **4**, 107133 (2014).
- [52] See Supplemental Material at <http://link.aps.org/supplemental/10.1103/PhysRevB.109.184402> for the detail of calculation method.